Rotational arrest in a repulsive colloidal glass

2006 J. Phys.: Condens. Matter 18 10119

(http://iopscience.iop.org/0953-8984/18/45/001)

INSTITUTE OF PHYSICS PUBLISHING JOURNAL OF PHYSICS: CONDENSED MATTER

J. Phys.: Condens. Matter **18** (2006) 10119–10132 doi:10.1088/0953-8984/18/45/001

Rotational arrest in a repulsive colloidal glass

G Mériguet, E Dubois, V Dupuis and R Perzynski

Université Pierre et Marie Curie—Paris 6, Laboratoire Liquides Ioniques et Interfaces Chargées, UMR 7612 (UPMC/CNRS/ESPCI)—Case 51, 4 Place Jussieu, 75252 Paris cedex 05, France

E-mail: meriguet@ccr.jussieu.fr

Received 7 June 2006, in final form 14 September 2006
Published 26 October 2006
Online at stacks.iop.org/JPhysCM/18/10119

Abstract

The rotational dynamics of aqueous colloidal dispersions of magnetic nanoparticles is examined whilst increasing the volume fraction up to the formation of a macroscopic solid. The freezing of the rotation is studied by magneto-optical relaxation experiments and related to small-angle neutron-scattering results showing that the structure, albeit imposed by the Coulombic repulsion, remains amorphous because of the size polydispersity. The volume fraction at which the freezing occurs is noticeably dependent on the salinity of the suspension. The latter point is discussed together with the microscopic mechanism of the arrest.

(Some figures in this article are in colour only in the electronic version)

1. Introduction

Since the pioneering work of Pusey [1, 2], a growing interest in the colloidal glass transition has arisen. As a result, numerous experimental and theoretical works have been carried out on this subject (for a review see [3]). However, so far, even if the rotational properties of molecular glasses have been deeply investigated thanks to dielectric relaxation experiments [4–6], few results have been obtained on the evolution of the rotational properties of colloidal particles throughout the glass transition. Götze *et al*, using the mode coupling theory (MCT), considered the rotational properties of an elongated probe in a simple glassy liquid and observed that for small elongations the rotational relaxation occurs by substantial angular steps and departs from the standard MCT behaviour, the latter being recovered for large elongations [7]. Forced Rayleigh scattering (FRS) experiments [8] have been performed to determine both the translational and rotational dynamics of probe colloidal particles dispersed in a molecular glass forming fluid but no results are available concerning the colloidal glass transition. Some experimental results concerning anisotropic particles with a large aspect ratio, such as laponite, have been obtained, exhibiting a coupled behaviour between translational and rotational freezing [9]. Moreover, using depolarized dynamic light scattering (DDLS) [10] or time-resolved phosphorescence anisotropy (TPA) [11, 12], the study of the concentration

dependence of the rotational diffusion of colloidal hard spheres has already been carried out up to volume fractions as high as 0.55 [13] showing a decrease by a factor of two of the rotational diffusion coefficient. In addition, a similar behaviour, mainly governed by hydrodynamic friction, has also been observed using deuteron-NMR experiments [14] up to a volume fraction of 0.5. For all the latter studies, carried out in the fluid phase, no real rotational arrest has ever been observed for quasi-spherical colloidal particles. The following question remains to be answered: what happens to the rotational degree of motion of the nanoparticles when the translation freezes?

The application of the aforementioned relaxation techniques to colloidal particles usually requires the presence of a permanent dipole within the particle. Considering this, we choose to transpose this approach to magnetic systems, thereby investigating well-known nanoparticles bearing a permanent magnetic dipolar moment. As a result, the present study focuses on ferrofluids, i.e. dispersions of quasi-spherical magnetic nanoparticles. Previous works on ferrofluids [15] have shown that the interparticle interaction can be continuously varied and controlled. Indeed, the knowledge of the volume fraction Φ, the osmotic pressure Π and the ionic strength through the salt concentration, enables one to tailor the interparticle interaction and thus the main properties of the dispersions. However, since concentrated suspensions are dark, optical methods such as DDLS become very difficult to operate. Therefore, with the aim of observing the Brownian rotational relaxation of the particles, up to highly concentrated suspensions, an intrinsic property of the magnetic nanoparticles that links the magnetic dipole moment to a difference of optical index [16, 17] was used. Indeed, the relaxation of the so-called magneto-induced birefringence gives information on the rotational mobility of the nanoparticles. The dipole–dipole interaction is definitely expected to alter the rate of the orientational relaxation [18]. However, both the small size of the particles and the intrinsic magnetic properties lead to a rather weak dipolar coupling [19]. Indeed, for two nanoparticles in contact with a dipole moment of the order of 10^4 μ_B and a diameter of 10 nm, the dipolar interaction is of the order of 1.5 kT [19], which is far too small to originate a rotational freezing. The results obtained in the present study have then a wider extent than the ferrofluids domain and are relevant for charged nanoparticles dispersed in aqueous solutions.

The organization of the paper is as follows. In section 2, we describe the preparation of the magnetic nanoparticle dispersions. In section 3, we detail the experimental methods used in the present work, small-angle neutron-scattering (SANS) and magneto-optical birefringence, which give access respectively to positional and orientational properties. In section 4, the latter structural and dynamical properties of the particles are examined while the volume fraction of the suspensions is increased up to a solid glassy phase. Rather unexpectedly the structural freezing goes along with a freezing of the rotation of the nanoparticles. A significant dependence of the rotational arrest on the salinity is found and favours an interpretation based on an asymmetric charge distribution.

2. Materials: preparation of the ferrofluids

The magnetic fluids used in this study consist of maghemite (γ-Fe_2O_3) nanoparticles dispersed in water. The particles are synthesized following reference [20] by coprecipitation of $FeCl_2$ and $FeCl_3$ in an aqueous ammonia solution. At this stage, magnetite particles sensitive to air oxidation are obtained. A further oxidation step is performed using iron (III) nitrate in nitric acid and yields fully oxidized cationic maghemite particles dispersed in nitric acid at pH $= 1.2$. To ensure the colloidal stability of the suspension at pH $= 7$, impossible to achieve with bare particles since the surface groups are neutralized leading to the flocculation of the suspension, an additional electrostatic repulsion is introduced. The particles are coated by citrate molecules, using trisodium citrate, the carboxylate groups of which are fully ionized, providing a negative

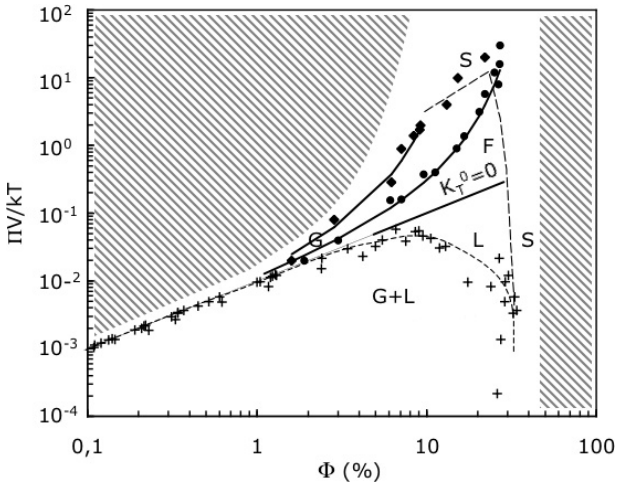

Figure 1. Phase diagram of the dispersions obtained from previous work (*crosses*) [22]. G = gas, L = liquid, F = fluid, S = '*macroscopic solid*'; the hatched regions cannot be reached. *Dashed lines*: coexistence or limit between phases. Particles A: *full circles*: [cit] = 0.03 mol l^{-1}; *full diamonds*: [cit] = 0.003 mol l^{-1}. *Solid lines*: effective hard spheres; the Carnahan–Starling expression of the osmotic pressure was used (see [15] and [23]).

Table 1. Particle properties derived by SANS, magnetization and magneto-optical birefringence experiments.

	V_w (nm^3)	d_w (nm)	m_s (A m^{-1})	d_0^{magn} (nm)	σ^{magn}	Δn_0	d_0^{bir} (nm)	σ^{bir}
Particles A	2.24×10^3	16.2	3.1×10^5	7	0.35	0.11	8.8	0.33
Particles B	1.0×10^3	12.4	3.1×10^5	8.6	0.23	0.07	9.2	0.23

surface charge of the particle at neutral pH. As this adsorption is a reversible phenomenon, free, i.e. non-adsorbed, citrate molecules have to be present in solution to prevent desorption. At the end of this stage, the diameter of the particle is of the order of 8 nm and follows a lognormal size distribution:

$$P(d) = \frac{1}{\sqrt{2\pi}\sigma d} \exp\left\{\frac{[\ln(d/d_0)]^2}{2\sigma^2}\right\}. \quad (1)$$

The size polydispersity after synthesis is of the order of $\sigma = 0.35$.

In order to prepare concentrated samples, we used the osmotic compression method. The suspension is poured in a dialysis bag, made of a semi-permeable cellulose membrane (Spectrapore, 12–14 kDa, i.e. about 3 nm porosity) retaining the nanoparticles but allowing the smaller molecules (water and ions) to cross the membrane. The closed bag is placed in a bath imposing the citrate concentration and the osmotic pressure thanks to a polymer (dextran $M = 110\,000$ g mol^{-1}, Fluka) the osmotic pressure of which is calibrated and does not depend on the salt concentration. To ensure that the osmotic equilibrium is reached, the duration of immersion is three weeks. The volume fraction of the particles is then determined thanks to a chemical titration of iron [21]. However, if the viscosity of the suspension is too large, the volume fraction is derived from the density of the suspension. The Π–Φ curves corresponding to two series of dispersions based on the same nanoparticles (particles A, see table 1) with different citrate concentrations are superimposed on the phase diagram of the suspension plotted in figure 1.

The screening effect of the free citrate concentration, proving the electrostatic nature of the repulsion, is clearly visible: at a given Φ, the lower the concentration of the salt, the stronger the repulsion, and hence the higher the pressure. In addition, figure 1 shows without doubt that the suspensions examined in the present study are on the whole repulsive. Indeed the osmotic pressure is far greater than the ideal one, i.e. with no interaction between particles, represented by the solid $K_T^0 = 0$ line, where K_T^0 is the dimensionless second virial coefficient. Last, at high volume fractions, a steep increase of the osmotic pressure is observed, as shown in figure 1, corresponding to a sudden change of macroscopic appearance: the suspension, fluid at small volume fractions, becomes viscous, pasty, rubber-like and finally solid and fragile like a window-glass. The latter samples, since no flow is observed within a week, will be referred to as '*macroscopic solids*' throughout the rest of this study. The threshold of this departure is strongly dependent on the free citrate concentration.

So far we have shown that well-characterized magnetic nanoparticles dispersions are synthesised and that the control of the volume fraction Φ, the osmotic pressure Π and the sodium citrate concentration [cit] enables us to adjust the interparticle interactions and to locate the dispersions under study precisely in the phase diagram of figure 1. All the suspensions are examined right after the preparation so that no ageing difference appears between the samples.

3. Experimental methods

3.1. Small-angle neutron scattering

In order to resolve the local structure of the suspension and the interparticle interaction, small-angle neutron-scattering (SANS) experiments were performed. They were carried out at the Institut Laue-Langevin (Grenoble) on instrument D11 at a 7 Å wavelength, the detector position being 2 and 8 m from the sample holder, corresponding to the wavevector range 0.005–0.16 Å^{-1}. The solvent used was light water, offering a strong contrast with the particle, the magnetic scattering from the particle being then negligible compared to the nuclear contribution [24]. Without an external magnetic field, the scattered intensity is isotropic and can be radially averaged leading to $I(q)$. The particles being nearly spherical, $I(q)$ is then written as

$$I(q)\ (\text{cm}^{-1}) = \Phi V_\text{w} (\Delta\rho)^2 P(q) S(q)$$

where V_w is the weight-averaged volume of the scatterers, $\Delta\rho$ is the difference of scattering length density between the particles and the solvent (contrast) and equals 7.5×10^{10} cm^{-2} for maghemite particles in light water, $P(q)$ is the form factor depending on the shape of the particle and $S(q)$ is the structure factor accounting for the interparticle organization. $P(q)$ is experimentally determined from dilute samples spectra for which interactions are negligible leading to $S_\text{dil}(q) \sim 1$ and $I_\text{dil}(q) = \Phi_\text{dil} V_\text{w} (\Delta\rho)^2 P(q)$. The weight-averaged volume V_w of the nanoparticles used in the present work and the corresponding diameter d_w, determined in the $q \to 0$ limit, are reported in table 1.

The structure factor $S(q)$ of concentrated suspensions is calculated using the following relation:

$$S(q, \Phi) = \Phi_\text{dil} I(q) / \Phi I_\text{dil}(q).$$

In the thermodynamic limit ($q \to 0$), the structure factor identifies with the isothermal osmotic compressibility of the suspension χ_T, whereas the position q_max of the peak of the structure factor S_max is related to the most probable interparticle distance.

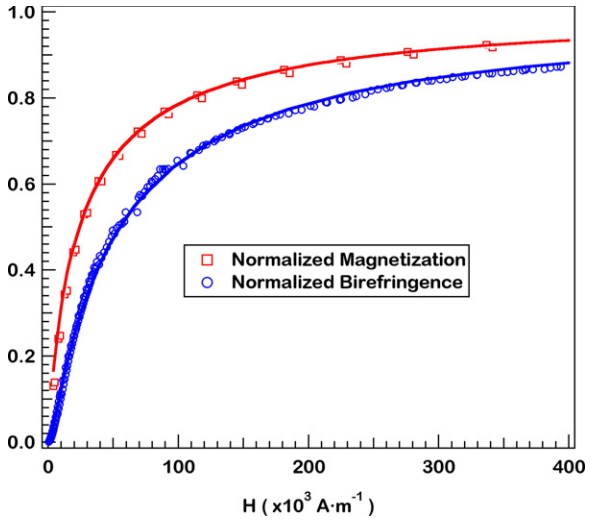

Figure 2. Normalized magnetization (M/M_s) and birefringence ($\Delta n/\Delta n_s$) data versus magnetic field for a dilute suspension (particles A, $\Phi = 1\%$). Lines are the corresponding fit functions.

3.2. Magnetic and magneto-optical experiments

As described in the introduction, each nanoparticle bears a permanent magnetic dipole and thus exhibits a magnetization when submitted to external magnetic field, the dipole aligning in the field direction. For dilute enough samples, i.e. for which interparticle interaction can be neglected, the magnetization obeys the first Langevin law $M(\xi) = \Phi m_s \mathcal{L}_1(\xi)$ with $\mathcal{L}_1(\xi) = 1/\tanh(\xi) - 1/\xi$ and ξ is the Langevin parameter, $\xi = \mu_0 \mu H/kT$. The magnetization is measured experimentally using a vibrating magnetometer [25] and then fitted by the first Langevin law weighted by a log-normal size distribution. This way we determine the magnetization of the particles m_s and the parameters of the distribution d_0^{magn} and σ^{magn}. The experimental data and the fit are plotted in figure 2; the parameters deduced from the fit are reported in table 1.

In addition to the magnetic dipole moment, every particle possesses a uniaxial optical anisotropy [26]. The dipole moment is linked to the optical axis by the magnetic anisotropy energy. For the maghemite particles considered here, the anisotropy energy is of the order of a few kTs [27]; the dipole is then not fixed to the optical axis of the particle but fluctuates around it (*soft dipole* compared to *rigid dipole*). Besides, the characteristic Néel relaxation time of the dipole along the optical axis is of the order of magnitude of 10^{-9}–10^{-8} s. Without an external field, no spontaneous orientation resulting in measurable magnetization or birefringence is observed. Nevertheless, when an external magnetic field is applied to the dispersion, not only the magnetic moment orientates along the field direction but the whole particle rotates, giving rise to a macroscopic birefringence Δn, the optical axis being aligned in the field direction on average. The magneto-induced birefringence is measured using the experimental setup described in [26]. For intermediate values of the external field, the orientation along the field direction competes with the thermal energy. For dilute samples, the birefringence data can be well described by the second Langevin law, $\Delta n(\xi) = \Delta n_s \mathcal{L}_2(\xi)$, where $\mathcal{L}_2(\xi) = 1$–$3\,\mathcal{L}_1(\xi)/\xi$ and ξ is the aforementioned Langevin parameter [28]. The intrinsic particle birefringence δn_0 is derived from the saturation value since $\Delta n_s = \delta n_0 \cdot \Phi$. The experimental values are reported in figure 2 together with magnetization for the sake of comparison. The size distribution

parameters, d_0^{bir} and σ^{bir}, as well as δn_0, are estimated in a straightforward manner by weighting the second Langevin law with the log-normal size distribution and fitting the experimental data as explained in [26] and in the same way as the analysis carried out on magnetization measurements. The values corresponding to the particles under study are reported in table 1.

The observed discrepancy among the sizes derived from different experiments and reported in table 1 stems mainly from the properties probed by each one of these techniques. Either the magnetization or the birefringence measurement can probe the entire size distribution since the orientation of one particle directly depends on its size and on the magnitude of the external field. Yet the size deduced from the birefringence is bigger than the size derived from the magnetization, for the contribution of small particles in the birefringence signal is weak compared to larger particles [26]. For SANS, the diameter obtained in the $q \rightarrow 0$ limit is a weight-averaged value corresponding then to a higher moment of the distribution and shifting the observed size to larger values [28] than the sizes extracted from the two former techniques.

3.3. Rotational relaxation

The rotational relaxation of the nanoparticles can be monitored by recording the relaxation of the magneto-induced birefringence signal. Indeed, the birefringence response of the suspension to a small external field (about 7.9 kA m^{-1}) pulse is a transient orientation followed by a relaxation to a randomly orientated state. A weak magnetic field is used in the experimental setup [29] in order to enable a fast switching off and limit induction effects. For ideal samples, i.e. monodisperse and dilute (independent particles), the relaxation of the birefringence is described by a monoexponential decay according to Perrin's law [30, 31]. The characteristic time is $\tau_{\mathrm{R}} = 3\eta V_{\mathrm{H}}/kT$, where η is the solvent viscosity and V_{H} the hydrodynamic volume of the particle. Experimentally, a monoexponential decay is measured if the size polydispersity is less then 0.2. For larger values, the size polydispersity of the samples induces a polydispersity of the relaxation time τ_{R}; hence a departure from the ideal monoexponential decay is observed, even for dilute dispersion, if the size polydispersity is not small enough. For a dilute dispersion of particles A with a volume fraction close to $\Phi \sim 1\%$ with a mean diameter of $d_0 = 7$ nm and a polydispersity of $\sigma = 0.35$, a relaxation time of $\tau_{\mathrm{R}} = 4\ \mu$s is measured.

4. Results and discussion

The volume fraction of the dispersion was increased up to the solid phase and both the positional and orientational properties were studied. The structure factors of different volume fractions are reported for dispersions of particles A with citrate concentrations of 0.03 mol l^{-1} in figure 3 (left) and 0.003 mol l^{-1} in figure 3 (right).

For the fluid samples at [cit] = 0.03 mol l^{-1} displayed on the left of figure 3, it is noticeable that, as the volume fraction increases, the compressibility decreases while the peak intensity increases, illustrating the globally repulsive interparticle interactions.

The right-hand side of figure 3 compares two concentrated dispersions of particles A; the first one is still a fluid whereas the second is a '*macroscopic solid*'. The '*macroscopic solid*' samples exhibit a liquid-like structure corresponding to an amorphous glass structure. This observation is consistent with the theoretical predictions of the absence of coexistence of a crystalline solid phase and a liquid phase, if the polydispersity is above a threshold of about 12% [32, 33]. Indeed the experimental polydispersity is close to 30%, as reported in table 1. Yet, for the '*macroscopic solid*' samples, the peak intensity is stunningly found to be lower than in the concentrated liquid phase even if the peak position is, as expected, shifted towards higher wavevectors, i.e. smaller most probable distances. This effect, although small in figure 3,

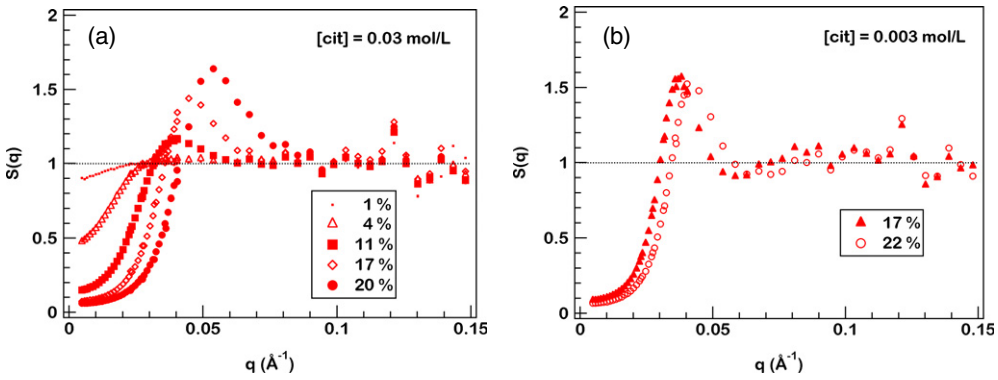

Figure 3. *Left*: structure factors for fluid dispersions of increasing volume fractions (see legend), at [cit] = 0.03 mol l^{-1} (particles A). *Right*: structure factors for concentrated fluid dispersions at [cit] = 0.003 mol l^{-1} (particles A; black triangles $\Phi = 17\%$ fluid, white circles $\Phi = 22\%$ '*macroscopic solid*').

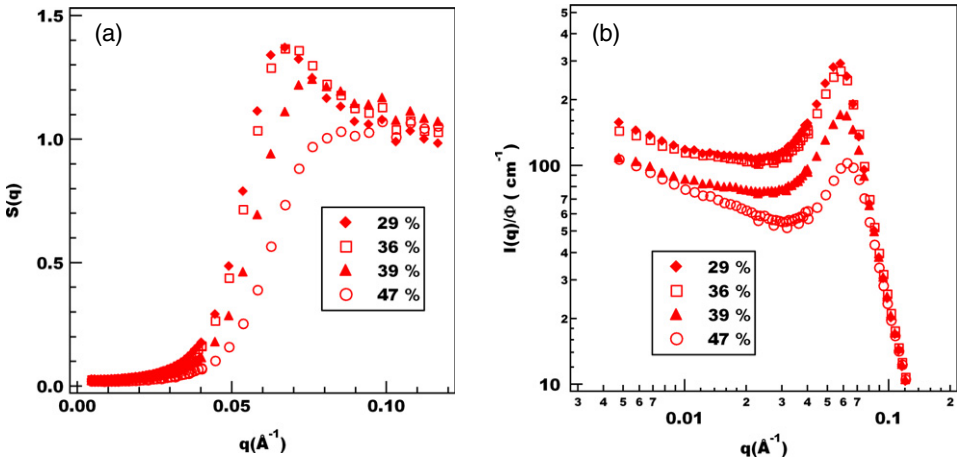

Figure 4. Structure factors (*left*) and reduced scattered intensities (*right*) for concentrated fluid dispersions (particles B) at [cit] = 0.03 mol l^{-1} for a series of volume fractions (see legend box). All samples are '*macroscopic solids*' apart from the one with $\Phi = 29\%$.

is systematic and is observed whatever the size of the nanoparticles or the citrate concentration. For example, the same trend for '*macroscopic solids*' is found for different particles as in [34]. Moreover, figure 4 displays the structure factors and the scattered intensities for concentrated fluid dispersions of nanoparticles B exhibiting the same phenomenon.

The observed collapse of the peak of the structure factor and of the scattered intensity with the increasing volume fraction might be accounted for by a segregation of the suspension into microdomains with different densities and polydispersities. Such a segregation would lead to a scattering from an inhomogeneous medium causing the observed smoothing of the peaks. Indeed, theoretical studies [35] and molecular dynamics simulations [36] have shown that the polydispersity induces a fractionation of the suspension containing clusters or microdomains of small and fast particles on the one hand and large and slow ones on the other hand. This segregation phenomenon is supposed to give rise to dynamic heterogeneities.

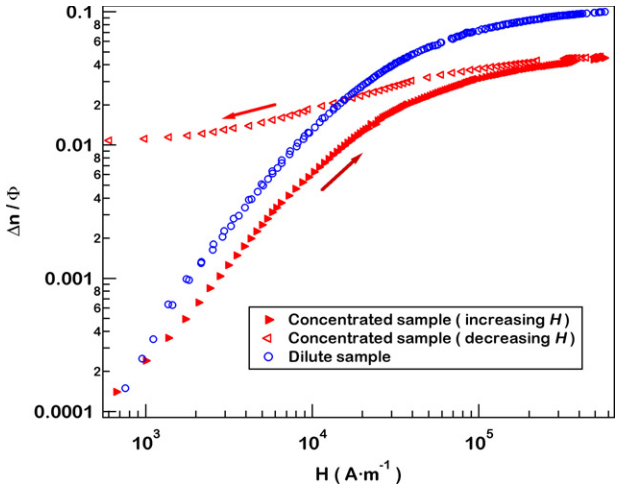

Figure 5. Static birefringence Δn divided by the volume fraction Φ as a function of the magnetic field for a concentrated dispersion (particles A $\Phi = 22.1\%$ and $[\text{cit}] = 0.03$ mol l^{-1}). *Solid triangles*: increasing H. *Hollow triangles*: decreasing H. *Circles*: dilute sample ($\Phi = 1\%$, same sample as in figure 2).

For the concentrated suspensions, the orientational properties are also altered; a hysteresis of the magneto-optical birefringence can be observed as shown in figure 5: particles remain orientated when the field is decreased.

As a result, the above-mentioned positional disorder (cf figure 3 *right* and figure 4 for example) in the concentrated samples is accompanied by a rotational slowing down. Furthermore, for such concentrated suspensions, the measured maximum of birefringence $\Delta n_{\max}$ is found to be lower than the expected saturation value ($\Delta n_s = \delta n_0 \Phi$). In figure 5, the measured birefringence during the field increase is always smaller than the ideal value obtained for a dilute sample where all the particles can freely align. The rotation of particles is then hindered, and whatever the magnetic field used to orientate the particles, the rotational dynamics is slower than the experiment duration, that is of the order of 30 min. The orientation of the nanoparticles is partially frozen. In order to follow the progressive freezing with the increase of volume fraction, the evolution of the ratio $\Delta n_{\max}/\Delta n_s$ for different samples based on nanoparticles A series is plotted in figure 6.

This magneto-optical experiment shows that, beyond a threshold of volume fraction close to 10%, the nanoparticles cannot be completely aligned in the field direction any longer at the timescale of the experiment. Furthermore, an effect of the interparticle isotropic repulsion is observed: the rotational freezing is stronger when the interparticle repulsion increases.

To complete this picture of the rotational freezing in high magnetic field at a timescale of 30 min, a study of the orientational relaxation is carried out under a small field. The evolution of the birefringence relaxation with the volume fraction is plotted in figure 7 for nanoparticles A at $[\text{cit}] = 0.03$ mol l^{-1}.

Up to a volume fraction of 11%, the relaxation depends weakly on Φ. Then, a steep slowing down is observed just before the macroscopic solidification of the sample, in the same way as the viscosity divergence observed during the glass transition of molecular systems. Moreover, for '*macroscopic solid*' samples, small relaxation times are observed again, as one can notice on the right-hand side of figure 7.

Whatever the volume fraction of the suspension under study, the ideal Perrin relaxation law is not appropriate. However, the decay can be fitted by a sum of a monoexponential accounting

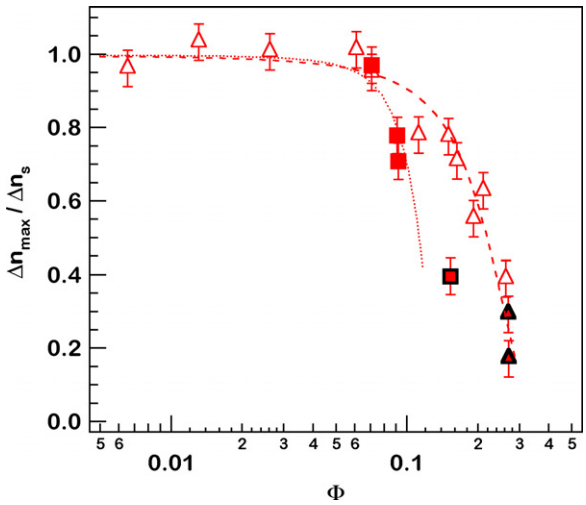

Figure 6. Static birefringence Δn_s at $H = 10\,500$ Oe $= 840$ kA m^{-1} normalized by the calculated value $\Delta n_s = \delta n_0 \Phi$, as a function of Φ (particles A). *Triangles*: [cit] $= 0.03$ mol l^{-1}. *Squares*: [cit] $= 0.003$ mol l^{-1}. The circumscribed symbols correspond to '*macroscopic solid*' samples. The lines are guides to the eyes.

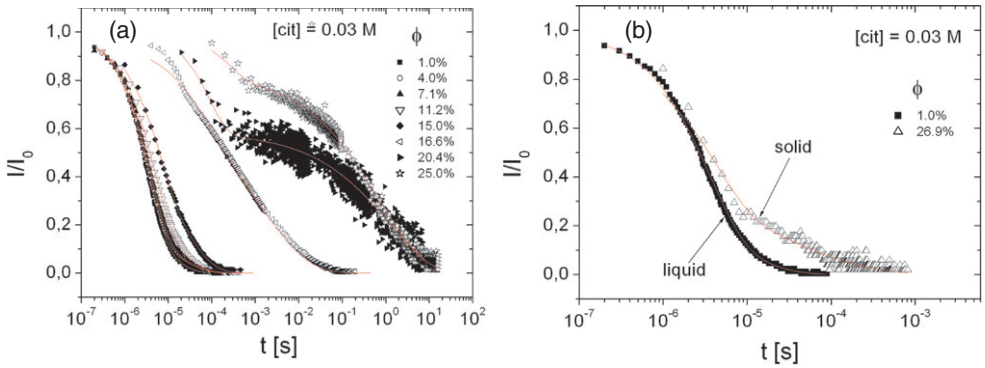

Figure 7. Evolution of the normalized optical intensity ($I(t)/I(t = 0)$ proportional to the birefringence) for [cit] $= 0.03$ mol l^{-1} (particles A). *Left*: effect of increase of the volume fraction of nanoparticles. *Right*: comparison between the relaxations of a dilute and a '*macroscopic solid*' sample.

for the short-time relaxation and a stretched exponential (Kolrausch–William–Watts function) with exponent $\alpha < 1$ accounting for the long-time behaviour:

$$I(t) = I_1 \exp\left(-\frac{t}{\tau_1}\right) + I_2 \exp\left(-\left(\frac{t}{\tau_2}\right)^{\alpha}\right)$$

where $I_1 + I_2 = I_0 = I(t = 0)$. α is related to the width of the relaxation time distribution: the smaller α, the wider the distribution. The reported intensities have been corrected from the optical absorption of the suspension and divided by Φ hereafter in all graphs.

First, a glance at the two intensity components I_1/Φ and I_2/Φ, reported in figure 8 for nanoparticles A and two concentrations of sodium citrate, gives a valuable insight into the phenomenon.

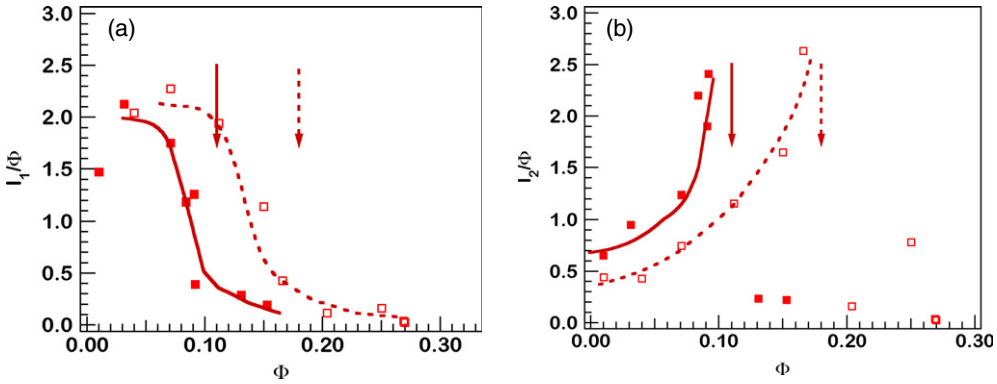

Figure 8. Variation of the intensities divided by the volume fraction of the two modes of relaxation of the birefringence versus the volume fraction. *Solid squares*: [cit] = 0.003 mol l^{-1}; *Hollow squares*: [cit] = 0.03 mol l^{-1} (particles A). The arrows point the threshold volume fraction Φ^* (see text).

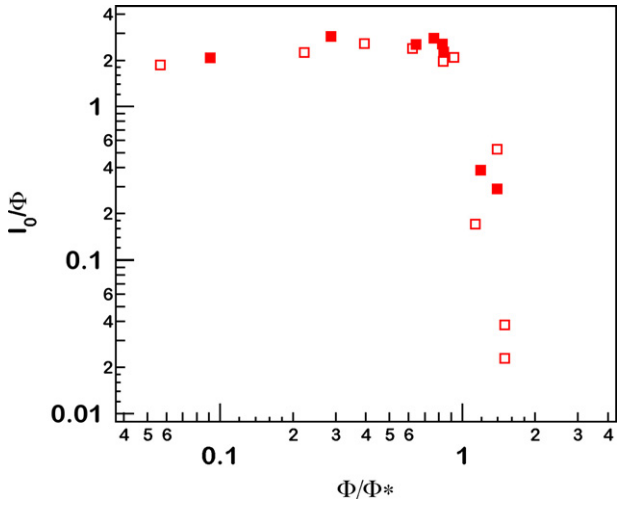

Figure 9. Variation of the initial total birefringence intensity at $t = 0$ divided by the volume fraction versus the ratio Φ/Φ^* (particles A).

From figure 8, one can define a threshold volume fraction Φ^* above which both contributions to the total intensity plummet drastically. According to figure 8, Φ^* not only depends on the nanoparticle size distribution but also on the citrate concentration. For nanoparticles A, it is taken here as $\Phi^* = 0.18$ for [cit] = 0.03 mol l^{-1} and $\Phi^* = 0.11$ for [cit] = 0.003 mol l^{-1}. Once the volume fraction is rescaled as Φ/Φ^*, the universal slowing down is unambiguous, as exhibited in figure 9.

Besides, the evolution of relaxation time τ_2, corresponding to the slow mode and extracted from the fit, is reported versus the ratio Φ/Φ^* in figure 10, together with the stretched exponential exponent α.

As one can see in figure 10, the rotational dynamics slow down by orders of magnitude, from microseconds to seconds. The increase of the relaxation times is relatively smooth for small volume fractions and then in the vicinity of $\Phi = \Phi^*$ a dramatically steep increase

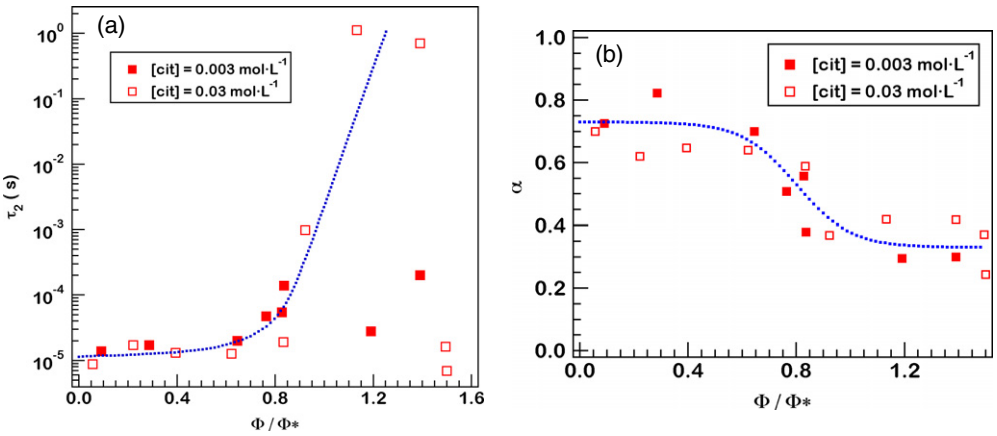

Figure 10. *Left*: variation of the relaxation time τ_2 with the reduced volume fraction Φ/Φ^* (particles A). *Right*: variation of the exponent α of the stretched exponential contribution to the relaxation versus Φ/Φ^* (particles A). The dotted lines are guides to the eyes.

followed by a decrease is observed. In addition, the evolution of the exponent α of the stretched exponential which is related to the width of the relaxation time distribution (the smaller α, the wider the distribution), exhibits a significant decrease around $\Phi = \Phi^*$.

For small volume fractions ($\Phi < 0.5\Phi^*$), particles can freely rotate even if the hydrodynamic friction and above all the cooperative orientation (as shown by recent Brownian dynamics numerical simulations [18]) are slowing down the relaxation. In this range, the polydispersity of the long-time relaxation, exhibited by the departure of α from 1, can be accounted for by the size polydispersity of the nanoparticles. For more concentrated suspensions, the influence of the neighbouring particles becomes predominant and the slowing down is abrupt around Φ^*. It leads, within a variation of the volume fraction of the order of 0.02–0.04, to an arrest of the orientational dynamics with a noticeable fall of the birefringence intensity, as one can see in figures 8 and 9. It comes with a significant broadening of the relaxation time distribution. For $\Phi > \Phi^*$, figures 7 and 10 show that small values of τ_2 can be recovered, albeit with a little intensity and a poor quality of fit. The relaxation is then likely logarithmic and history dependent. This phenomenon is confined to the '*macroscopic solid*' samples inside which a minority of particles may rotate relatively freely while the majority are either trapped or relax with a time larger than the duration of the experiment. Such dynamical heterogeneities would be supported by the heterogeneous structure suggested by SANS (see figures 3 and 4). Another explanation might be the rotational counterpart of the caging phenomenon. That is to say, for short times, the particles may still rotate partially, the extent of rotation being limited by the cage of the surrounding particles. For longer times, when the surrounding particles move, the rotation can proceed further.

To gain information on the concentrated regime ($\Phi > \Phi^*$), where slow dynamics is observed, the time allowed to the particles to orientate, i.e. the duration of the applied field pulse, has been varied. The results for a sample with $\Phi/\Phi^* = 1.4$ ($\Phi = 0.25$ and $[\text{cit}] = 0.03$ mol l^{-1}) are reported in figure 11.

The measured relaxation times increase with the duration of the magnetic field pulse. This observation gives an insight of the relaxation times distribution (note that it is not an absolute evidence of ageing of the sample). Definitely, a short pulse of orientation cannot activate all the times of the relaxation time distribution that are longer than the pulse duration. The relaxation

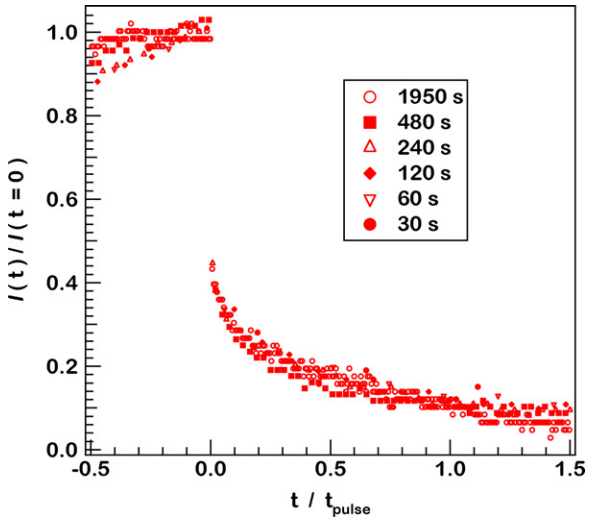

Figure 11. Influence of the duration of the magnetic field pulse on the orientational relaxation ($\Phi/\Phi^* = 1.4$: $\Phi = 0.25$ and [cit] = 0.03 mol l^{-1}, particles A). The pulse durations are reported in the legend box. For the sake of clarity, only one point out of ten is plotted.

time distribution is truncated with a higher boundary that equals the duration of the pulse; consequently, the longer the pulse, the wider the relaxation time distribution probed and the longer the mean relaxation time observed. This phenomenon is illustrated by the merging of all curves when the data are plotted versus t/t_{pulse}, as one can see in figure 11.

In summary, for $\Phi/\Phi^* < 0.5$, the suspensions are moderately concentrated fluids, where for example the virial expansion is valid. For $0.5 < \Phi/\Phi^* < 1$, the suspensions are still fluid, yet a noticeable slowing down of the rotational dynamics is observed together with a widening of the relaxation time distribution. Above $\Phi/\Phi^* = 1$, the rotational degrees of freedom is partially frozen; the dispersions are either glass-forming fluids or '*macroscopic solids*'.

Since the particles are quasi-spherical, the microscopic mechanism of the rotational freezing remains to be understood. For perfectly spherical particles three hypotheses can be suggested: dipolar interactions, hydrodynamic friction, and contact between particles. The latter can be rapidly excluded since the isotropic repulsion is strong enough to prevent the contact for the suspensions. Then the dipolar contribution is, as stated beforehand, too weak to be the main origin of this phenomenon. Finally the hydrodynamic friction for a particle in a spherical cavity has been evaluated in [37] and shows an increase of the order of 30% for $\Phi = 0.30$, that is to say an effect far too small to account for the freezing observed here. Actually, Degiorgio *et al* in [13] only observe a decrease by a factor of two of the short-time rotational diffusion coefficient at $\Phi = 0.55$ for hard spheres, a far less significant effect than the one observed in the present work. Moreover, for charged spherical silica particles, it was found that decreasing the salt concentration and enhancing in this manner the interparticle repulsion, maintaining the particles away from each other, decreases the hydrodynamic coupling [12]. Indeed, the larger the interparticle distance, the smaller the hydrodynamic hindrance to the rotation.

Furthermore, the small shape anisotropy of the particles, for example, is not responsible for the freezing since, when the liquid–solid transition occurs, the particles are rather far from each other according to the moderate volume fraction and the SANS spectra. The strong electrostatic repulsion keeps the particles away from each another, minimizing the consequences of the small

shape anisotropy. The increase of this repulsion shifts the threshold of the freezing to lower values of volume fraction in contradiction with this hypothesis.

Eventually, the faceting of the particles might lead to an anisotropic charge distribution on the surface and, consequently, an anisotropic electrical double layer around the particles. This effect might be accountable for the freezing observed with these nanoparticles and is to be compared to results obtained with very low ionic strength dispersion of anisotropic laponite particles at small volume fractions [9]. The latter hypothesis is strengthened by the fact that the electrostatic interaction governs the volume fraction threshold Φ^*.

In order to shed some light on the dynamics of these ferrofluids, complementary experiments have been carried out in the concentrated region: the translational dynamics and its ageing for $\Phi/\Phi^* = 1.2$ have been probed by x-ray photon correlation spectroscopy [38] and the study of ageing for rotation is in progress. All the degrees of freedom of the particles, translation and rotation, are frozen around Φ^*. Besides, these magnetic nanoparticles exhibit the so-called superspin glass behaviour [39] with a critical temperature T_g around 150 K [40].

5. Conclusion

A rotational arrest has been evidenced in colloidal magnetic dispersions using magneto-optical birefringence relaxation and small-angle neutron-scattering. Within a small percentage of volume fraction, the relaxation time tends to diverge with a simultaneous dramatic fall of the number of the rotating particles. At the same time, the macroscopic solidification of the samples is witnessed. The threshold Φ^* around which this arrest is observed is strongly dependent on the intensity of the interparticle repulsion, tuned by the free salt concentration in the present work. The microscopic mechanism is still to be determined even if the purely hydrodynamic or the dipole–dipole interparticle interactions can be excluded. More likely, the faceting of the particles generates an anisotropic counterion distribution. The latter anisotropy may induce a geometrical frustration, which, in addition to the sample polydispersity, prevents the crystallization and accounts for the observed freezing. This assumption is supported by recent results of molecular dynamics simulations [41]. Finally, above Φ^*, an ageing process seems to occur and is currently under investigation together with the coupling of the rotational and translational freezing for these suspensions.

Acknowledgments

The authors gratefully thank Bela Farago for experimental support on the small-angle neutron spectrometer D11 at the Institut Laue-Langevin (Grenoble) and the referee for fruitful comments.

References

[1] Pusey P N and van Megen W 1986 *Nature* **320** 340–2
[2] Pusey P N 1991 *Liquids, Freezing and the Glass Transition* (*Les Houches Session 51, 1989*) ed D Levesque, J-P Hansen and J Zinn-Justin (Amsterdam: North-Holland)
[3] Cipelletti L and Ramos L 2005 *J. Phys.: Condens. Matter* **17** R253–5
[4] Leheny R L and Nagel S R 1998 *Phys. Rev.* B **57** 5154
[5] Miller M A, Jimenez-Ruiz M, Bermejo F J and Birge N O 1998 *Phys. Rev.* B **57** R13977
[6] Colla E V, Chao L K and Weissman M B 2001 *Phys. Rev.* B **63** 134107
[7] Götze W, Singh A P and Voigtmann Th 2000 *Phys. Rev.* E **61** 6934–49
[8] Kanetakis J and Sillescu H 1996 *Chem. Phys. Lett.* **252** 127–34
[9] Jabbari-Farouji S, Eiser E, Wegdam G H and Bonn D 2004 *J. Phys.: Condens. Matter* **16** L471–7

[10] Piazza R, Degiorgio V, Corti M and Stavans J 1990 *Phys. Rev.* B **42** 4885
[11] Koenderink G H, Zhang H, Letting M P, Nägele G and Philipse A P 2001 *Phys. Rev.* E **64** 022401
[12] Koenderink G H, Zhang H, Aarts D G A L, Letting M P, Philipse A P and Nägele G 2003 *Faraday Discuss.* **123** 335–54
[13] Degiorgio V, Piazza R and Jones R B 1995 *Phys. Rev.* E **52** 2707–17
[14] Kanetakis J, Tölle A and Sillescu H 1996 *Phys. Rev.* E **55** 3006–14
[15] Cousin F, Dubois E and Cabuil V 2003 *Phys. Rev.* E **68** 021405
[16] Majorana Q 1902 *C. R. Acad. Sci. Paris* **135** 159–61
[17] Bacri J-C, Dumas J, Gorse D, Perzynski R and Salin D 1985 *J. Physique Lett.* **46** 1199
[18] Mériguet G, Jardat M and Turq P 2005 *J. Chem. Phys.* **123** 144915
[19] Holm C and Weis J-J 2005 *Curr. Opin. Colloid Interface Sci.* **5** 133–40
[20] Massart R 1980 *C. R. Acad. Sci. Paris* **291** 1–2
[21] Charlot G 1966 *Les Méthodes de la Chimie Analytique* (Paris: Masson et Cie)
[22] Dubois E, Perzynski R, Boué F and Cabuil V 2000 *Langmuir* **13** 5617
[23] Cousin F, Dubois E, Cabuil V, Boué F and Perzynski R 2001 *Braz. J. Phys.* **31** 350
[24] Gazeau F, Boué F, Dubois E and Perzynski R 2003 *J. Phys.: Condens. Matter* **15** S1305–34
[25] Foner S and Macniff E J 1968 *Rev. Sci. Instrum.* **39** 171–9
[26] Hasmonay E, Dubois E, Bacri J-C, Perzynski R, Raikher Yu L and Stepanov V I 1998 *Eur. Phys. J.* B **5** 859–67
[27] Gazeau F, Bacri J-C, Gendron F, Perzynski R, Raikher Yu L, Stepanov V I and Dubois E 1998 *J. Magn. Magn. Mater.* **186** 175–87
[28] Berkovsky B 1996 *Magnetic Fluids and Applications Handbook* (New York: Begell House)
[29] Hasmonay E, Bée A, Bacri J-C and Perzynski R 1999 *J. Phys. Chem.* B **103** 6421–8
[30] Perrin F 1928 *Ann. Sci. Ecole Norm. S* **45** 1–51
[31] Perrin F 1934 *J. Phys. Radium* **5** 497–511
[32] Bolhuis P G and Kofke D A 1996 *J. Phys.: Condens. Matter* **8** 9627–31
[33] Bartlett P 2000 *J. Phys.: Condens. Matter* **12** A275–80
[34] Mériguet G, Dubois E, Bourdon A, Demouchy G, Dupuis V and Perzynski R 2005 *J. Magn. Magn. Mater.* **289** 39–42
[35] Fasolo M and Sollich P 2004 *Phys. Rev.* E **70** 041410
[36] Sears R P 2000 *J. Chem. Phys.* **113** 4732–9
[37] General Discussion 2003 *Faraday Discuss.* **123** 401–8
[38] Robert A, Wandersman E, Dubois E, Dupuis V and Perzynski R 2006 *Europhys. Lett.* **75** 764–70
[39] Mørup S, Bødker F, Hendriksen P V and Lindenroth S 1995 *Phys. Rev.* B **52** 287–94
[40] Parker D, Ladieu F, Vincent E, Mériguet G, Dubois E, Dupuis V and Perzynski R 2005 *J. Appl. Phys.* **97** 10A502
[41] Shintani H and Tanaka H 2006 *Nat. Phys.* **2** 200